Camera Calibration from Surfaces of Revolution

Kwan-Yee K. Wong, Paulo R. S. Mendonça and Roberto Cipolla

Kwan-Yee K. Wong (corresponding author) is with the Department of Computer Science and Information Systems, The University of Hong Kong, Pokfulam Road, Hong Kong. E-mail: kykwong@csis.hku.hk. tel: +852 2857 8443. fax: +852 2559 8447. Paulo R. S. Mendonça is with GE Global Research Center, Schenectady, NY 12301, USA. E-mail: mendonca@crd.ge.com. tel: +1 518 387 5321. Roberto Cipolla is with the Department of Engineering, University of Cambridge, Cambridge CB2 1PZ, United Kingdom. E-mail: cipolla@eng.cam.ac.uk. tel: +44 1223 332849. fax: +44 1223 332662

Abstract

This paper addresses the problem of calibrating a pinhole camera from images of a surface of revolution. Camera calibration is the process of determining the intrinsic or internal parameters (i.e., aspect ratio, focal length and principal point) of a camera, and it is important for both motion estimation and metric reconstruction of 3D models. In this paper a novel and simple calibration technique is introduced, which is based on exploiting the symmetry of images of surfaces of revolution. Traditional techniques for camera calibration involve taking images of some precisely machined calibration pattern (such as a calibration grid). The use of surfaces of revolution, which are commonly found in daily life (e.g., bowls and vases), makes the process easier as a result of the reduced cost and increased accessibility of the calibration objects. In this paper, it is shown that two images of a surface of revolution will provide enough information for determining the aspect ratio, focal length and principal point of a camera with fixed intrinsic parameters. The algorithms presented in this paper have been implemented and tested with both synthetic and real data. Experimental results show that the camera calibration method presented here is both practical and accurate.

Keywords

Camera Calibration, Surface of Revolution, Harmonic Homology, Absolute Conic, Vanishing Point.

I. INTRODUCTION

An essential step for motion estimation and 3D Euclidean reconstruction, two important tasks in computer vision, is the determination of the intrinsic parameters of cameras. This process, known as *camera calibration*, usually involves taking images of some special pattern with known geometry, extracting the features from the images, and minimizing their reprojection errors. Details of such calibration algorithms can be found in [1], [2], [3], [4], [5, Chapter 7] and [6, Chapter 3]. These methods do not require direct mechanical measurements on the cameras, and often produce very good results. Nevertheless, they involve the design and use of highly accurate tailor-made calibration patterns, which are often both difficult and expensive to be manufactured.

In this paper a novel technique for camera calibration is introduced. It relates the idea of calibration from vanishing points [7], [8], [9] to the symmetry properties exhibited in the silhouettes of surfaces of revolution [10], [11], [12], [13], [14]. The method presented here allows the camera to be calibrated from two or more silhouettes of surfaces of revolution (like bowls and vases, etc.), which are commonly found in daily life. The use of such objects has the advantages of easy accessibility and low cost, in contrast to traditional calibration patterns.

This paper is organized as follows. Section II gives a literature survey on existing camera calibration techniques. Section III defines the camera model used and gives brief reviews on camera calibration from vanishing points and the symmetry properties associated with the silhouettes of surfaces of revolution. These provide the theoretical background needed for the camera calibration method [15] introduced in Section IV. The algorithms and implementation details are given in Section V, followed by a discussion of the singular cases and an error analysis in Section VI and VII. Section VIII first presents results of experiments conducted on synthetic data, which are used to perform an evaluation on the robustness of the algorithms in the presence of noise. Experiments on real data then show the usefulness of the proposed method. Finally, conclusions are given in Section IX.

II. Previous Works

Classical calibration techniques [16], [17], [18] in photogrammetry involve full-scale nonlinear optimizations with large number of parameters. These techniques are able to cope with complex camera models and they produce accurate results, but require a good initialization and are computationally expensive. In [19], Abdel-Aziz and Karara presented the *direct linear transformation* (DLT) technique, which is one of the most commonly used calibration techniques in the field of computer vision. By ignoring lens distortion and treating the coefficients of the 3×4 projection matrix as unknowns, DLT only involves solving a system of linear equations, which can be done by a linear least-squares method. In practice, the linear solution obtained from DLT is usually refined iteratively by minimizing the reprojection errors of the 3D reference points [1], [6]. In [2], [3], Tsai and Lenz introduced the *radial alignment constraint* (RAS) and developed a technique which also accounts for lens distortion.

All the calibration techniques mentioned so far require the knowledge of the 3D coordinates of a certain number of reference points and their corresponding image coordinates. In [7], Caprile and Torre showed that, under the assumption of zero skew and unit aspect ratio, it is possible to calibrate a camera from the vanishing points associated with three mutually orthogonal directions. This idea was further elaborated in [8], [9] to develop practical systems for reconstructing architectural scenes. In contrast to traditional calibration techniques, these methods depend only on the presence of some special structures, but not on the exact geometry of those structures.

The theory of *self-calibration* was first introduced by Maybank and Faugeras [20], who es-

tablished the relationship between camera calibration and the epipolar transformation via the *absolute conic* [6]. Implementation of the theory in [20], together with real data experiments, were given by Luong and Faugeras [21] for fixed intrinsic parameters. In [22], Triggs introduced the *absolute quadric* and gave a simpler formulation which can easily incorporate any constraint on the intrinsic parameters. Based on [22], a practical technique for self-calibration of multiple cameras with varying intrinsic parameters was developed by Pollefeys et al. in [23]. Specialized methods of self-calibration have also been derived when the camera motion is restricted to pure rotation [24] or planar motion [25].

The calibration technique introduced in this paper, namely *calibration from surfaces of revolution*, falls into the same category as calibration from vanishing points (see fig. 1). Like calibration from vanishing points, which only requires the presence of three mutually orthogonal directions, the technique presented here only requires the calibration target to be a surface of revolution, but the exact geometry of the surface is not important. An important problem not addressed in this paper is how to detect surfaces of revolution in an image, so that they can be used in the calibration algorithm. A practical solution to this has been presented by Zisserman et al. in [13]. The technique developed in that paper is based on the same symmetry properties exploited here, and works well even in the presence of partial occlusion and clustered background.

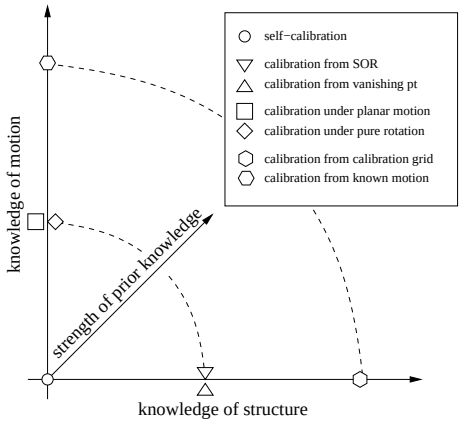

Fig. 1. Different categories of camera calibration techniques.

III. Theoretical Background

A. Camera Model

In this paper, a camera is modelled as a pinhole (perspective) camera and the imaging process can be expressed as

$$\alpha \begin{bmatrix} u \\ v \\ 1 \end{bmatrix} = \mathbf{P} \begin{bmatrix} X \\ Y \\ Z \\ 1 \end{bmatrix}, \tag{1}$$

where (X, Y, Z) are the coordinates of a 3D point $\mathbf{X}$, (u, v) are the image coordinates of the projection of $\mathbf{X}$, and α is an arbitrary scale factor. $\mathbf{P}$ is a 3×4 matrix known as the *projection matrix* [26], which models the pinhole camera. The projection matrix $\mathbf{P}$ is not a general 3×4 matrix, but has a special structure given by [6]

$$\mathbf{P} = \mathbf{K}[\mathbf{R}\ \mathbf{t}], \tag{2}$$

where $\mathbf{K}$ is a 3×3 upper triangular matrix known as the *camera calibration matrix*, $\mathbf{R}$ is a 3×3 rotation matrix and $\mathbf{t}$ is a 3×1 translation vector. $\mathbf{R}$ and $\mathbf{t}$ are called the *extrinsic parameters* [6] of the camera, and they represent the rigid body transformation between the camera and the scene (see fig. 2). The camera calibration matrix $\mathbf{K}$ has the form [6]

$$\mathbf{K} = \begin{bmatrix} f_u & \varsigma & u_0 \\ 0 & f_v & v_0 \\ 0 & 0 & 1 \end{bmatrix} = \begin{bmatrix} af & \varsigma & u_0 \\ 0 & f & v_0 \\ 0 & 0 & 1 \end{bmatrix}, \tag{3}$$

where f is the *focal length*, $a = f_u/f_v$ is the aspect ratio and ς is the *skew* which depends on the angle between the image axes. (u_0, v_0) is called the *principal point*, and it is the point at which the optical axis (z_c-axis) intersects the image plane (see fig. 2). The focal length, aspect ratio, skew and principal point are referred to as the *intrinsic parameters* [6] of the camera, and *camera calibration* is the process of estimating these parameters. If the image axes are orthogonal to each other, which is often the case, ς will be equal to zero. In practice, the aspect ratio and skew of a camera are often assumed to be one and zero, respectively, to reduce the dimension of the search space in camera calibration. This generally speeds up the calibration process and makes the results more stable. Such an initial estimate of the intrinsic parameters can be further refined

later by relaxing the unit aspect ratio and zero skew constraints. A camera is said to be calibrated if its intrinsic parameters are known. If both the intrinsic and extrinsic parameters of a camera are known, then the camera is said to be fully calibrated.

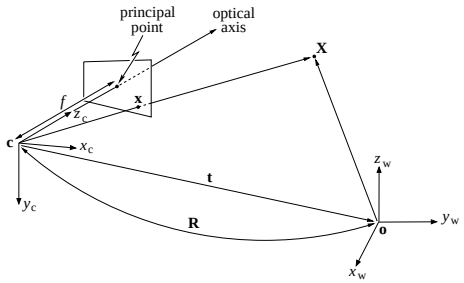

Fig. 2. The extrinsic parameters of a camera represent the rigid body transformation between the world coordinate system (centered at **o**) and the camera coordinate system (centered at **c**), and the intrinsic parameters represent the camera internal parameters like focal length, aspect ratio, skew and principal point.

B. Calibration from Vanishing Points

In [7], Caprile and Torre showed that under the assumption of zero skew and unit aspect ratio, the principal point of a camera will coincide with the orthocenter of a triangle with vertices given at three vanishing points from three mutually orthogonal directions. Such properties of the vanishing points, together with the symmetry properties associated with the silhouettes of surfaces of revolution, will be used later in Section IV to derive a simple technique for camera calibration. A simple derivation of Caprile and Torre's result is given below.

Consider a pinhole camera with focal length f, unit aspect ratio, zero skew and principal point $\tilde{\mathbf{x}}_0$. The vector from the camera center to any point $\tilde{\mathbf{x}}$ on the image plane, in camera coordinate system, is given by $[(\tilde{\mathbf{x}} - \tilde{\mathbf{x}}_0)^{\mathrm{T}}\ f]^{\mathrm{T}}$. Let $\tilde{\mathbf{v}}_q$, $\tilde{\mathbf{v}}_r$ and $\tilde{\mathbf{v}}_s$ be three vanishing points associated with three mutually orthogonal directions $\mathbf{N}_q$, $\mathbf{N}_r$ and $\mathbf{N}_s$ respectively. The three vectors from the camera center to $\tilde{\mathbf{v}}_q$, $\tilde{\mathbf{v}}_r$ and $\tilde{\mathbf{v}}_s$ will be mutually orthogonal to each other, and hence

$$(\tilde{\mathbf{v}}_q - \tilde{\mathbf{x}}_0) \cdot (\tilde{\mathbf{v}}_r - \tilde{\mathbf{x}}_0) + f^2 = 0, \tag{4}$$

$$(\tilde{\mathbf{v}}_r - \tilde{\mathbf{x}}_0) \cdot (\tilde{\mathbf{v}}_s - \tilde{\mathbf{x}}_0) + f^2 = 0, \tag{5}$$

$$(\tilde{\mathbf{v}}_s - \tilde{\mathbf{x}}_0) \cdot (\tilde{\mathbf{v}}_q - \tilde{\mathbf{x}}_0) + f^2 = 0. \tag{6}$$

Subtracting (6) from (4) gives

$$(\tilde{\mathbf{v}}_q - \tilde{\mathbf{x}}_0) \cdot (\tilde{\mathbf{v}}_r - \tilde{\mathbf{v}}_s) = 0. \tag{7}$$

Equation (7) shows that $\tilde{\mathbf{x}}_0$ lies on a line passing through $\tilde{\mathbf{v}}_q$ and orthogonal to the line joining $\tilde{\mathbf{v}}_r$ and $\tilde{\mathbf{v}}_s$. Similarly, subtracting (4) from (5) and (5) from (6) gives

$$(\tilde{\mathbf{v}}_r - \tilde{\mathbf{x}}_0) \cdot (\tilde{\mathbf{v}}_s - \tilde{\mathbf{v}}_q) = 0, \quad (8)$$

$$(\tilde{\mathbf{v}}_s - \tilde{\mathbf{x}}_0) \cdot (\tilde{\mathbf{v}}_q - \tilde{\mathbf{v}}_r) = 0. \quad (9)$$

Equations (7)–(9) imply that the principal point $\tilde{\mathbf{x}}_0$ coincides with the orthocenter of the triangle with vertices $\tilde{\mathbf{v}}_q$, $\tilde{\mathbf{v}}_r$ and $\tilde{\mathbf{v}}_s$. Besides, equations (4)–(6) show that the focal length f is equal to the square root of the product of the distances from the orthocenter to any vertex and to the opposite side (see fig. 3). As a result, under the assumption of zero skew and unit aspect ratio, it is possible to estimate the principal point and the focal length of a camera using vanishing points from three mutually orthogonal directions. A similar derivation was also presented by Cipolla et al. in [8].

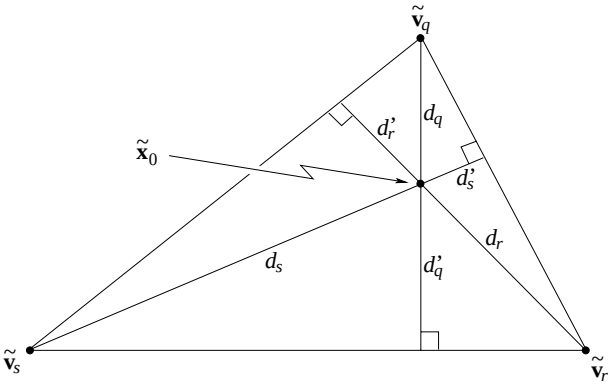

Fig. 3. The principal point $\tilde{\mathbf{x}}_0$ of the camera coincides with the orthocenter of the triangle with vertices given at the vanishing points $\tilde{\mathbf{v}}_q$, $\tilde{\mathbf{v}}_r$ and $\tilde{\mathbf{v}}_s$ associated with three mutually orthogonal directions, and the focal length of the camera is given by $f = \sqrt{d_q d_q'} = \sqrt{d_r d_r'} = \sqrt{d_s d_s'}$.

C. Symmetry in Surfaces of Revolution

As will be shown in the next paragraph, the silhouette of a surface of revolution, viewed under a pinhole camera, will be invariant to a harmonic homology [13]. Such properties of the silhouette can be exploited to calibrate the intrinsic parameters of a camera, as will be shown in Section IV. A simple proof of such symmetry properties is given below, which also shows that the axis of the associated harmonic homology is given by the image of the revolution axis,

and that the center of the homology is given by the vanishing point corresponding to the normal direction of the plane containing the axis of revolution and the camera center.

Consider a surface of revolution $\mathbf{S}_{\mathrm{r}}$, whose axis of revolution coincides with the y-axis, being viewed by a pinhole camera $\hat{\mathbf{P}} = [\mathbb{I}_3 \ \ -\mathbf{c}]$ centered at $\mathbf{c} = [0 \ 0 \ \ -d_z]^{\mathrm{T}}$, with $d_z > 0$ (see fig. 4). By symmetry considerations, it is easy to see that the silhouette $\hat{\rho}$ of $\mathbf{S}_{\mathrm{r}}$ formed on the image plane will be bilaterally symmetric about the image of the revolution axis $\hat{\mathbf{l}}_{\mathrm{s}} = [1 \ 0 \ 0]^{\mathrm{T}}$. The lines of symmetry (i.e., lines joining symmetric points in $\hat{\rho}$) will be parallel to the normal $\mathbf{N}_x = [1 \ 0 \ 0 \ 0]^{\mathrm{T}}$ of the plane Π_{s} that contains the axis of revolution and the camera center, and the vanishing point associated with $\mathbf{N}_x$ is given by $\hat{\mathbf{v}}_x = [1 \ 0 \ 0]^{\mathrm{T}}$. The bilateral symmetry exhibited in $\hat{\rho}$ can be described by the transformation [27], [28]

$$\begin{aligned} \mathbf{T} &= \begin{bmatrix} -1 & 0 & 0 \\ 0 & 1 & 0 \\ 0 & 0 & 1 \end{bmatrix} \\ &= \mathbb{I}_3 - 2\frac{\hat{\mathbf{v}}_x \hat{\mathbf{l}}_{\mathrm{s}}^{\mathrm{T}}}{\hat{\mathbf{v}}_x^{\mathrm{T}} \hat{\mathbf{l}}_{\mathrm{s}}}. \end{aligned} \tag{10}$$

Note that the transformation $\mathbf{T}$ is a *harmonic homology* (see Appendix, and also [29], [30] for details) with axis $\hat{\mathbf{l}}_{\mathrm{s}}$ and center $\hat{\mathbf{v}}_x$, which maps every point in $\hat{\rho}$ to its symmetric counterpart in $\hat{\rho}$. The silhouette $\hat{\rho}$ is thus said to be invariant to the harmonic homology $\mathbf{T}$ (i.e., $\hat{\rho} = \mathbf{T}\hat{\rho}$).

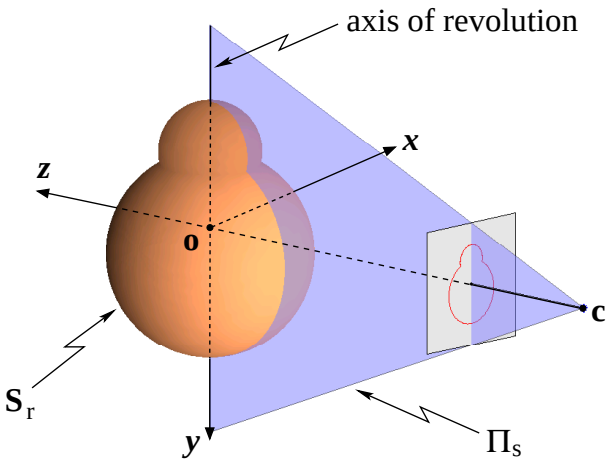

Fig. 4. A surface of revolution $\mathbf{S}_{\mathrm{r}}$, whose axis of revolution coincides with the y-axis, being viewed by a pinhole camera $\hat{\mathbf{P}} = [\mathbb{I}_3 \ \ -\mathbf{c}]$ centered at $\mathbf{c} = [0 \ 0 \ \ -d_z]^{\mathrm{T}}$.

Now consider an arbitrary pinhole camera $\mathbf{P}$ by introducing the intrinsic parameters repre-

sented by the camera calibration matrix $\mathbf{K}$ to $\hat{\mathbf{P}}$, and by applying the rotation $\mathbf{R}$ to $\hat{\mathbf{P}}$ about its optical center. Hence $\mathbf{P} = \mathbf{KR}[\mathbb{I}_3 \ -\mathbf{c}]$ or $\mathbf{P} = \mathbf{H}\hat{\mathbf{P}}$, where $\mathbf{H} = \mathbf{KR}$. Let $\mathbf{x}$ be the projection of a 3D point $\mathbf{X}$ in $\mathbf{P}$, hence

$$\begin{aligned} \mathbf{x} &= \mathbf{PX} \\ &= \mathbf{H}\hat{\mathbf{P}}\mathbf{X} \\ &= \mathbf{H}\hat{\mathbf{x}}, \end{aligned} \tag{11}$$

where $\hat{\mathbf{x}} = \hat{\mathbf{P}}\mathbf{X}$. Equation (11) implies that the 3×3 matrix $\mathbf{H}$ represents a planar homography which transforms the image formed by $\hat{\mathbf{P}}$ into the image formed by $\mathbf{P}$. Similarly, $\mathbf{H}^{-1}$ transforms the image formed by $\mathbf{P}$ into the image formed by $\hat{\mathbf{P}}$. The silhouette ρ of $\mathbf{S}_\mathrm{r}$, formed on the image plane of $\mathbf{P}$, can thus be obtained by applying the planar homography $\mathbf{H}$ to $\hat{\rho}$ (i.e., $\rho = \mathbf{H}\hat{\rho}$). Let $\hat{\mathbf{x}}$ and $\hat{\mathbf{x}}'$ be a pair of symmetric points in $\hat{\rho}$, and $\mathbf{x} = \mathbf{H}\hat{\mathbf{x}}$ and $\mathbf{x}' = \mathbf{H}\hat{\mathbf{x}}'$ be their correspondences in ρ. The symmetry between $\hat{\mathbf{x}}$ and $\hat{\mathbf{x}}'$ is given by

$$\hat{\mathbf{x}}' = \mathbf{T}\hat{\mathbf{x}}. \tag{12}$$

Substituting $\hat{\mathbf{x}}$ and $\hat{\mathbf{x}}'$ in (12) by $\mathbf{H}^{-1}\mathbf{x}$ and $\mathbf{H}^{-1}\mathbf{x}'$, respectively, gives [27], [28]

$$\begin{aligned} (\mathbf{H}^{-1}\mathbf{x}') &= \mathbf{T}(\mathbf{H}^{-1}\mathbf{x}) \\ \mathbf{x}' &= \mathbf{HTH}^{-1}\mathbf{x} \\ &= \mathbf{H}(\mathbb{I}_3 - 2\frac{\hat{\mathbf{v}}_x\hat{\mathbf{l}}_\mathrm{s}^\mathrm{T}}{\hat{\mathbf{v}}_x^\mathrm{T}\hat{\mathbf{l}}_\mathrm{s}})\mathbf{H}^{-1}\mathbf{x} \\ &= (\mathbb{I}_3 - 2\frac{\mathbf{v}_x\mathbf{l}_\mathrm{s}^\mathrm{T}}{\mathbf{v}_x^\mathrm{T}\mathbf{l}_\mathrm{s}})\mathbf{x}, \end{aligned} \tag{13}$$

where $\mathbf{v}_x = \mathbf{H}\hat{\mathbf{v}}_x$, and $\mathbf{l}_\mathrm{s} = \mathbf{H}^{-\mathrm{T}}\hat{\mathbf{l}}_\mathrm{s}$. Note that $\mathbf{v}_x$ is the vanishing point corresponding to the normal direction $\mathbf{N}_x$ in $\mathbf{P}$, and $\mathbf{l}_\mathrm{s}$ is the image of the revolution axis of $\mathbf{S}_\mathrm{r}$ in $\mathbf{P}$. Let $\mathbf{W} = \mathbf{HTH}^{-1}$ be the harmonic homology with axis $\mathbf{l}_\mathrm{s}$ and center $\mathbf{v}_x$. Equation (13) shows that $\mathbf{W}$ will map each point in ρ to its symmetric counterpart in ρ, and hence ρ is invariant to the harmonic homology $\mathbf{W}$ (i.e., $\rho = \mathbf{W}\rho$).

In general, the harmonic homology $\mathbf{W}$ has four degrees of freedom. When the camera is pointing directly towards the axis of revolution, the harmonic homology will reduce to a *skew symmetry* [31], [32], [33], [34], where the vanishing point $\mathbf{v}_x$ is at infinity. The skew symmetry

can be described by the transformation

$$\mathbf{S} = \frac{1}{\cos(\phi-\theta)} \begin{bmatrix} -\cos(\phi+\theta) & -2\cos\phi\sin\theta & 2d_{\mathrm{l}}\cos\phi \\ -2\sin\phi\cos\theta & \cos(\phi+\theta) & 2d_{\mathrm{l}}\sin\phi \\ 0 & 0 & \cos(\phi-\theta) \end{bmatrix}, \tag{14}$$

where $d_{\mathrm{l}} = u_0\cos\theta + v_0\sin\theta$. The image of the revolution axis and the vanishing point are given by $\mathbf{l}_{\mathrm{s}} = [\cos\theta \ \ \sin\theta \ \ -d_{\mathrm{l}}]^{\mathrm{T}}$ and $\mathbf{v}_x = [\cos\phi \ \ \sin\phi \ \ 0]^{\mathrm{T}}$ respectively, and $\mathbf{S}$ has only three degrees of freedom. If the camera also has zero skew and unit aspect ratio, the transformation will then become a *bilateral symmetry*, given by

$$\mathbf{B} = \begin{bmatrix} -\cos 2\theta & -\sin 2\theta & 2d_{\mathrm{l}}\cos\theta \\ -\sin 2\theta & \cos 2\theta & 2d_{\mathrm{l}}\sin\theta \\ 0 & 0 & 1 \end{bmatrix}. \tag{15}$$

While $\mathbf{l}_{\mathrm{s}}$ will have the same form as in the case of skew symmetry, the vanishing point will now be at infinity and will have a direction orthogonal to $\mathbf{l}_{\mathrm{s}}$. As a result, $\mathbf{B}$ has only two degrees of freedom. These three different cases of symmetry are illustrated in fig. 5.

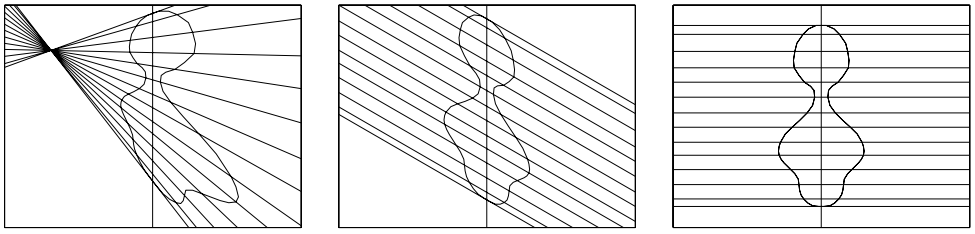

(a) (b) (c)

Fig. 5. (a) Silhouette of a surface of revolution under general viewing conditions. The symmetry of the silhouette is described by a harmonic homology defined by the image of the revolution axis and a vanishing point. (b) When the camera is pointing directly towards the axis of revolution, the transformation reduces to a skew symmetry, which is a particular case of the harmonic homology where the vanishing point is at infinity. (c) If the camera also has zero skew and unit aspect ratio, the transformation becomes a bilateral symmetry, in which the vanishing point is at infinity and has a direction orthogonal to the image of the revolution axis.

IV. Camera Calibration

A. Vanishing Points and the Harmonic Homology

Consider a surface of revolution $\mathbf{S}_{\mathrm{r}}$ viewed by a pinhole camera $\mathbf{P} = \mathbf{K}[\mathbf{R} \ \ \mathbf{t}]$. Let ρ be the silhouette of $\mathbf{S}_{\mathrm{r}}$, $\mathbf{l}_{\mathrm{s}}$ be the image of the revolution axis of $\mathbf{S}_{\mathrm{r}}$, and $\mathbf{v}_x$ be the vanishing point

corresponding to the normal direction $\mathbf{N}_x$ of the plane Π_{s} that contains the revolution axis of $\mathbf{S}_{\mathrm{r}}$ and the camera center of $\mathbf{P}$. The silhouette ρ is then invariant to the harmonic homology $\mathbf{W}$ with axis $\mathbf{l}_{\mathrm{s}}$ and center $\mathbf{v}_{\mathrm{x}}$ (see Section III-C).

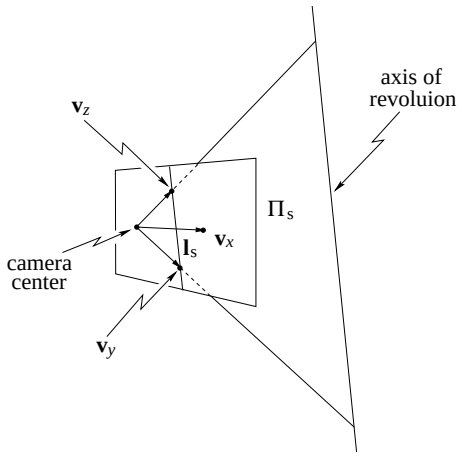

Fig. 6. Three mutually orthogonal directions associated with a surface of revolution.

Consider now any two vectors $\mathbf{N}_y$ and $\mathbf{N}_z$ parallel to the plane Π_{s} and orthogonal to each other, which together with $\mathbf{N}_x$ form a set of three mutually orthogonal directions (see fig. 6). Under the assumption of zero skew and unit aspect ratio, the vanishing points associated with these three directions can be used to determine the principal point and the focal length of $\mathbf{P}$, as shown in Section III-B. By construction, the vanishing points $\mathbf{v}_y$ and $\mathbf{v}_z$, corresponding to the directions $\mathbf{N}_y$ and $\mathbf{N}_z$ respectively, will lie on the image of the revolution axis $\mathbf{l}_{\mathrm{s}}$. Given the harmonic homology $\mathbf{W}$ associated with ρ, with an axis given by the image of the revolution axis $\mathbf{l}_{\mathrm{s}}$ and a center given by the vanishing point $\mathbf{v}_x$, the principal point $\mathbf{x}_0$ of $\mathbf{P}$ will therefore lie on a line $\mathbf{l}_x$ passing through $\mathbf{v}_x$ and orthogonal to $\mathbf{l}_{\mathrm{s}}$, and the focal length f will be equal to the square root of the product of the distances from the principal point $\mathbf{x}_0$ to $\mathbf{v}_x$ and to $\mathbf{l}_{\mathrm{s}}$ respectively (see fig. 7). As a result, given two or more silhouettes of surfaces of revolution, the principal point can be estimated as the intersection of the lines $\mathbf{l}_x$ and the focal length follows.

B. Pole-Polar Relationship and the Absolute Conic

Following the notations in the previous subsection, consider the equation of the plane Π_{s} which can be deduced from $\mathbf{P}$ and the image of the revolution axis $\mathbf{l}_{\mathrm{s}}$, and is given by

$$\Pi_{\mathrm{s}} \;=\; \mathbf{P}^{\mathrm{T}}\mathbf{l}_{\mathrm{s}}. \tag{16}$$

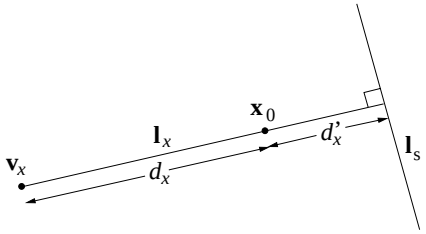

Fig. 7. The vanishing point $\mathbf{v}_x$ and the image of the revolution axis $\mathbf{l}_\mathrm{s}$ define a line $\mathbf{l}_x$ on which the principal point $\mathbf{x}_0$ must lie, and the focal length f is equal to $\sqrt{d_x d'_x}$.

By definition, $\mathbf{v}_x$ is the vanishing point corresponding to the normal direction $\mathbf{N}_x$ of the plane Π_s, and hence

$$\mathbf{v}_x \;=\; \mathbf{P}\mathbf{N}_x. \tag{17}$$

Now let $\mathbf{\Omega} = \begin{bmatrix} \mathbb{I}_3 & \mathbf{0}_3 \\ \mathbf{0}_3^\mathrm{T} & 0 \end{bmatrix}$ be the *absolute dual quadric* [22]. Observe that Π_s can be expressed as $\Pi_\mathrm{s} = [\mathbf{n}_x^\mathrm{T} \;\; -d]^\mathrm{T}$, where $\mathbf{n}_x$ is the normal direction of Π_s in Cartesian (non-homogeneous) coordinates. Therefore, $\mathbf{\Omega}\Pi_\mathrm{s} = [\mathbf{n}_x^\mathrm{T}\; 0]^\mathrm{T} = \mathbf{N}_x$, which allows equation (17) to be rewritten as

$$\begin{aligned} \mathbf{v}_x &= \mathbf{P}\mathbf{\Omega}\Pi_\mathrm{s} \\ &= \mathbf{P}\mathbf{\Omega}\mathbf{P}^\mathrm{T}\mathbf{l}_\mathrm{s} \\ &= \mathbf{K}\mathbf{K}^\mathrm{T}\mathbf{l}_\mathrm{s} \\ \mathbf{K}^{-\mathrm{T}}\mathbf{K}^{-1}\mathbf{v}_x &= \mathbf{l}_\mathrm{s} \\ \boldsymbol{\omega}\;\mathbf{v}_x &= \mathbf{l}_\mathrm{s}, \end{aligned} \tag{18}$$

where $\boldsymbol{\omega} = \mathbf{K}^{-\mathrm{T}}\mathbf{K}^{-1}$ is the projection of the absolute quadric in $\mathbf{P}$, known as the *image of the absolute conic*. Equation (18) gives the pole-polar relationship, with respect to the image of the absolute conic, between the vanishing point $\mathbf{v}_x$ of the normal direction of the plane Π_s and the vanishing line $\mathbf{l}_\mathrm{s}$ of Π_s [35]. By assuming the skew of $\mathbf{P}$ to be zero, expanding (18) gives

$$\begin{bmatrix} \frac{1}{f_u^2} & 0 & -\frac{u_0}{f_u^2} \\ 0 & \frac{1}{f_v^2} & -\frac{v_0}{f_v^2} \\ -\frac{u_0}{f_u^2} & -\frac{v_0}{f_v^2} & (\frac{u_0}{f_u})^2 + (\frac{v_0}{f_v})^2 + 1 \end{bmatrix} \mathbf{v}_x = \mathbf{l}_\mathrm{s}, \tag{19}$$

where f_u, f_v and (u_0,v_0) are the intrinsic parameters of $\mathbf{P}$. It follows that the harmonic homology associated with the silhouette of a surface of revolution will provide two constraints on the four

intrinsic parameters of a camera. As a result, under the assumption of fixed intrinsic parameters and zero skew, it is possible to calibrate a camera from two or more silhouettes of surfaces of revolution. Further, under the assumption of unit aspect ratio (i.e., $f_u = f_v$), it can be derived from equation (19) that the focal length f is equal to the square root of the product of the distances from the principal point (u_0, v_0) to the vanishing point $\mathbf{v}_x$ and to the image of the revolution axis $\mathbf{l}_\mathrm{s}$. These results agree with the analysis of the vanishing points in the previous subsection.

V. Algorithms and Implementations

A. Estimation of the Harmonic Homology

The silhouette ρ of a surface of revolution can be extracted from the image by applying a Canny edge detector [36] (see fig. 8). The harmonic homology $\mathbf{W}$ that maps each side of the silhouette ρ to its symmetric counterpart is then estimated by minimizing the geometric distances between the original silhouette ρ and its transformed version $\rho' = \mathbf{W}\rho$. This can be done by sampling N evenly spaced points $\mathbf{x}_i$ along the silhouette ρ and optimizing the cost function

$$\mathrm{Cost}_{\mathbf{W}}(\mathbf{v}_x, \mathbf{l}_\mathrm{s}) = \sum_{i=1}^{N} \mathrm{dist}(\mathbf{W}(\mathbf{v}_x, \mathbf{l}_\mathrm{s})\mathbf{x}_i, \rho)^2, \tag{20}$$

where $\mathrm{dist}(\mathbf{W}(\mathbf{v}_x, \mathbf{l}_\mathrm{s})\mathbf{x}_i, \rho)$ is the orthogonal distance from the transformed sample point $\mathbf{x}'_i = \mathbf{W}(\mathbf{v}_x, \mathbf{l}_\mathrm{s})\mathbf{x}_i$ to the original silhouette ρ.

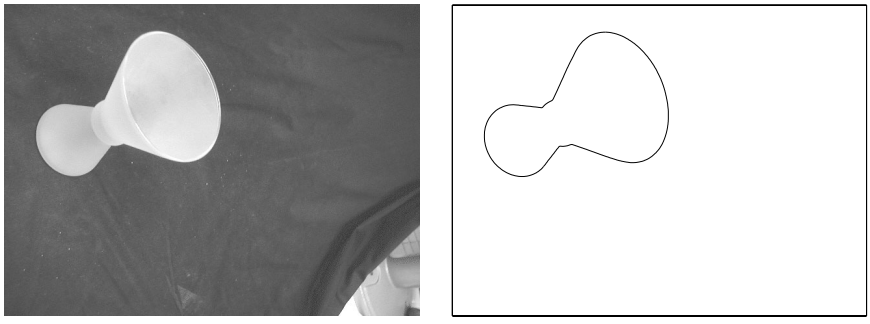

Fig. 8. The silhouette of a surface of revolution (candle holder) extracted by applying a Canny edge detector.

The success of most nonlinear optimization problems requires a good initialization so as to avoid convergence to local minima. This is achieved here by using bitangents of the silhouette [10]. Two points in the silhouette ρ near a bitangent are selected manually and the neighborhood of each point is transformed into a curve in the Hough space (see fig. 9). The bitangent and the

bitangent points can then be located by finding the intersection of the two transformed curves in the Hough space (see [37] for details).

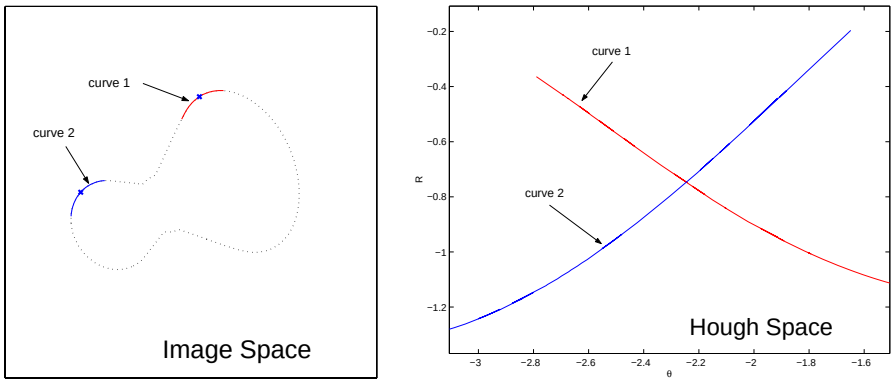

Fig. 9. Two points in the silhouette ρ near a bitangent are selected manually and the neighborhood of each point is transformed into a curve in the Hough space. The bitangent and the bitangent points can then be located by finding the intersection of the two transformed curves in the Hough space.

Consider two corresponding bitangents $\mathbf{l}_{\mathrm{b}}$ and $\mathbf{l}'_{\mathrm{b}}$ on the two sides of ρ, with bitangent points $\mathbf{x}_1$, $\mathbf{x}_2$ and $\mathbf{x}'_1$, $\mathbf{x}'_2$ respectively (see fig. 10). Let $\mathbf{l}_{\mathrm{d}}$ be the line joining $\mathbf{x}_1$ and $\mathbf{x}'_2$, and $\mathbf{l}'_{\mathrm{d}}$ be the line joining $\mathbf{x}'_1$ and $\mathbf{x}_2$. The intersection of $\mathbf{l}_{\mathrm{b}}$ with $\mathbf{l}'_{\mathrm{b}}$ and the intersection of $\mathbf{l}_{\mathrm{d}}$ with $\mathbf{l}'_{\mathrm{d}}$ define a line which will provide an estimate for the image of the revolution axis $\mathbf{l}_{\mathrm{s}}$. Let $\mathbf{l}_{\mathrm{c}}$ be the line joining $\mathbf{x}_1$ and $\mathbf{x}'_1$, and $\mathbf{l}'_{\mathrm{c}}$ be the line joining $\mathbf{x}_2$ and $\mathbf{x}'_2$. The intersection of $\mathbf{l}_{\mathrm{c}}$ with $\mathbf{l}'_{\mathrm{c}}$ will provide an estimate for the vanishing point $\mathbf{v}_x$. The initialization of $\mathbf{l}_{\mathrm{s}}$ and $\mathbf{v}_x$ from bitangents often provides an excellent initial guess for the optimization problem. This is generally good enough to avoid any local minimum and allows convergence to the global minimum in a small number of iterations. Note that bitangents are used here only to provide an initial estimate for $\mathbf{l}_{\mathrm{s}}$ and $\mathbf{v}_x$, which will be further refined by optimizing the cost function given in (20). As a result, error in the estimation of the bitangents will not directly affect the accuracy of the final estimation of the intrinsic parameters. Alternatively in the absence of any bitangents, $\mathbf{l}_{\mathrm{s}}$ can be initialized manually by observing the symmetry in the silhouette, and $\mathbf{v}_x$ can be initialized to be a point at infinity having a direction orthogonal to $\mathbf{l}_{\mathrm{s}}$.

The above approach of estimating the harmonic homology is similar to the one presented in [13]. However, the initialization using bitangent points allows for optimizing the full projective model, represented by the harmonic homology, in contrast to the affine approximation used in [13], which corresponds to a skew symmetry transformation. An alternative method, which

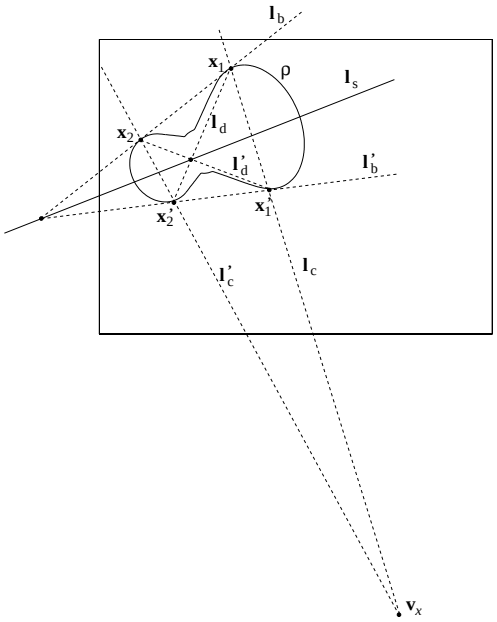

Fig. 10. Initialization of the optimization parameters $\mathbf{l}_{\mathrm{s}}$ and $\mathbf{v}_x$ from the bitangents and lines formed from the bitangent points.

computes the harmonic homology implicitly, was developed in [38]. The method presented here is much simpler than the one shown in [38], which relies on an unnecessarily complicated prediction, verification and selection scheme. An important point to note is that both the results in [13] and [38] demonstrate that the harmonic homology can be successfully computed in the presence of partial occlusion and clustered background.

B. Estimation of the Intrinsic Parameters

Method I:

Under the assumption of zero skew and unit aspect ratio, the line $\mathbf{l}_x$ passing through the principal point (u_0, v_0) and the vanishing point $\mathbf{v}_x$ will be orthogonal to the image of the revolution axis $\mathbf{l}_{\mathrm{s}}$ (see Section IV). Let $\mathbf{v}_x = [v_1 \ v_2 \ v_3]^{\mathrm{T}}$ and $\mathbf{l}_{\mathrm{s}} = [l_1 \ l_2 \ l_3]^{\mathrm{T}}$. The line $\mathbf{l}_x$ can be expressed in terms of $\mathbf{v}_x$ and $\mathbf{l}_{\mathrm{s}}$, and is given by

$$\mathbf{l}_x = \frac{1}{\sqrt{(l_2 v_3)^2 + (l_1 v_3)^2}} \begin{bmatrix} l_2 v_3 \\ -l_1 v_3 \\ l_1 v_2 - l_2 v_1 \end{bmatrix}. \tag{21}$$

Given two such lines $\mathbf{l}_{x1}$ and $\mathbf{l}_{x2}$, the principal point (u_0, v_0) will then be given by the intersection of $\mathbf{l}_{x1}$ with $\mathbf{l}_{x2}$. When more than two lines are available, the principal point (u_0, v_0) can be estimated by a linear least-squares method from

$$\begin{bmatrix} \mathbf{l}_{x1}^{\mathrm{T}} \\ \mathbf{l}_{x2}^{\mathrm{T}} \\ \vdots \\ \mathbf{l}_{xM}^{\mathrm{T}} \end{bmatrix} \begin{bmatrix} \alpha u_0 \\ \alpha v_0 \\ \alpha \end{bmatrix} = \mathbf{0}, \tag{22}$$

where $M \geq 2$ is the total number of lines (i.e., number of silhouettes) and α is a scale factor. The estimated principal point (u_0, v_0) is then projected onto each line $\mathbf{l}_{xi}$ orthogonally as $\mathbf{x}_{0i}$, and the focal length f will be given by

$$f = \frac{1}{M} \sum_{i=1}^{M} \sqrt{\mathrm{dist}(\mathbf{x}_{0i}, \mathbf{v}_{xi}) \times \mathrm{dist}(\mathbf{x}_{0i}, \mathbf{l}_{\mathrm{s}i})}, \tag{23}$$

where $\mathrm{dist}(\mathbf{x}_{0i}, \mathbf{v}_{xi})$ is the distance between $\mathbf{x}_{0i}$ and $\mathbf{v}_{xi}$, and $\mathrm{dist}(\mathbf{x}_{0i}, \mathbf{l}_{\mathrm{s}i})$ is the orthogonal distance from $\mathbf{x}_{0i}$ to the image of the revolution axis $\mathbf{l}_{\mathrm{s}i}$. Note that the terms for summation are the focal lengths estimated from each pair of $\mathbf{v}_{xi}$ and $\mathbf{l}_{\mathrm{s}i}$ with the estimated principal point projected onto the corresponding $\mathbf{l}_{xi}$ (see Section IV), and the focal length f is then taken to be the mean of these estimated values.

When the aspect ratio of the camera is known but not equal to one, there exists a planar homography $\mathbf{A}(a)$ that transforms the image into one that would have been obtained from a camera with the same focal length f, unit aspect ratio and principal point (u_0', v_0'). The homography $\mathbf{A}(a)$ is given by

$$\mathbf{A}(a) = \begin{bmatrix} \frac{1}{a} & 0 & -\frac{u_0}{a} + u_0' \\ 0 & 1 & -v_0 + v_0' \\ 0 & 0 & 1 \end{bmatrix}, \tag{24}$$

where a is the aspect ratio of the original camera, and (u_0, v_0) and (u_0', v_0') are the principal points of the original and transformed cameras respectively. By setting the principal point (u_0', v_0') of the transformed camera to $(u_0/a, v_0)$, the homography $\mathbf{A}(a)$ is reduced to

$$\mathbf{A}'(a) = \begin{bmatrix} \frac{1}{a} & 0 & 0 \\ 0 & 1 & 0 \\ 0 & 0 & 1 \end{bmatrix}. \tag{25}$$

The vanishing points $\mathbf{v}_{xi}$ and the images of the revolution axis $\mathbf{l}_{si}$ are transformed by $\mathbf{A}'(a)$ and $\mathbf{A}'^{-\mathrm{T}}(a)$ respectively, and equations (21)–(23) can then be applied to obtain the principal point (u_0', v_0') and the focal length f. Note that the principal point (u_0', v_0') obtained in this way is the principal point of the transformed camera, and the principal point (u_0, v_0) of the original camera is simply given by

$$\begin{bmatrix} u_0 \\ v_0 \end{bmatrix} = \begin{bmatrix} au_0' \\ v_0' \end{bmatrix}. \tag{26}$$

Method II:

When the aspect ratio of the camera is unknown, the camera can be calibrated by first estimating the image of the absolute conic $\boldsymbol{\omega}$. Let $\mathbf{v}_x = [v_1 \ v_2 \ v_3]^{\mathrm{T}}$ and $\mathbf{l}_{\mathrm{s}} = [l_1 \ l_2 \ l_3]^{\mathrm{T}}$. From (19), under the assumption of zero skew, each pair of $\mathbf{v}_x$ and $\mathbf{l}_{\mathrm{s}}$ will provide the following two constraints

$$v_1 l_3 \omega_1 + (v_3 l_3 - v_1 l_1)\omega_2 - v_2 l_1 \omega_4 - v_3 l_1 \omega_5 = 0, \text{ and} \tag{27}$$

$$v_1 l_2 \omega_2 - v_2 l_3 \omega_3 + (v_2 l_2 - v_3 l_3)\omega_4 + v_3 l_2 \omega_5 = 0, \tag{28}$$

where ω_i are the matrix elements of the absolute conic $\boldsymbol{\omega}$:

$$\boldsymbol{\omega} = \begin{bmatrix} \omega_1 & 0 & \omega_2 \\ 0 & \omega_3 & \omega_4 \\ \omega_2 & \omega_4 & \omega_5 \end{bmatrix}. \tag{29}$$

Hence the image of the absolute conic can be estimated, up to a scale factor, by a linear least-squares method when there are two or more pairs of $\mathbf{v}_x$ and $\mathbf{l}_{\mathrm{s}}$. After obtaining an estimate for $\boldsymbol{\omega}$, the camera calibration matrix $\mathbf{K}$ can then be obtained from $\boldsymbol{\omega}$ by Cholesky decomposition [39, Chapter 2]. Note that the unit aspect ratio constraint can also be easily incorporated by setting $\omega_1 = \omega_3$ in equations (28) and (29).

VI. Singular Cases

The algorithms presented in the previous section have two main steps: the computation of the harmonic homologies, and the subsequent computation of the camera intrinsic parameters using the just computed homologies. Therefore, the only two situations where the algorithms fail are when the homologies cannot be computed, and when the homologies do not provide enough

information for the calibration of the camera. The following subsections analyze the occurrence of these degeneracies.

A. Conic Silhouette

If the silhouette ρ of a surface of revolution is a conic, there will be an infinite number of harmonic homologies to which the silhouette ρ will be invariant. Such a situation results in a singular case for camera calibration from surfaces of revolution.

Consider a conic represented by a 3×3 symmetric matrix $\mathbf{C}$, such that every point $\mathbf{x}$ on the conic satisfies

$$\mathbf{x}^{\mathrm{T}}\mathbf{C}\mathbf{x} = 0. \tag{30}$$

Given a point $\mathbf{x}_{\mathrm{e}}$ outside the conic $\mathbf{C}$, two tangents can be drawn from $\mathbf{x}_{\mathrm{e}}$ to $\mathbf{C}$ (see fig. 11), and the line $\mathbf{l}_{\mathrm{e}}$ passing through the two tangent points is given by

$$\mathbf{l}_{\mathrm{e}} = \mathbf{C}\mathbf{x}_{\mathrm{e}}. \tag{31}$$

Let $\mathbf{W}_{\mathrm{e}}$ be a harmonic homology with axis $\mathbf{l}_{\mathrm{e}}$ and center $\mathbf{x}_{\mathrm{e}}$, i.e.,

$$\mathbf{W}_{\mathrm{e}} \;=\; \mathbb{I}_3 - 2\frac{\mathbf{x}_{\mathrm{e}}\mathbf{l}_{\mathrm{e}}^{\mathrm{T}}}{\mathbf{x}_{\mathrm{e}}^{\mathrm{T}}\mathbf{l}_{\mathrm{e}}}. \tag{32}$$

Substituting (31) into (32) gives

$$\mathbf{W}_{\mathrm{e}} \;=\; \mathbb{I}_3 - 2\frac{\mathbf{x}_{\mathrm{e}}\mathbf{x}_{\mathrm{e}}^{\mathrm{T}}\mathbf{C}^{\mathrm{T}}}{\mathbf{x}_{\mathrm{e}}^{\mathrm{T}}\mathbf{C}\mathbf{x}_{\mathrm{e}}}. \tag{33}$$

Let $\mathbf{x}$ be a point on $\mathbf{C}$ and $\mathbf{x}' = \mathbf{W}_{\mathrm{e}}\mathbf{x}$, and consider the equation

$$\begin{aligned} \mathbf{x}'^{\mathrm{T}}\mathbf{C}\mathbf{x}' &= (\mathbf{W}_{\mathrm{e}}\mathbf{x})^{\mathrm{T}}\mathbf{C}(\mathbf{W}_{\mathrm{e}}\mathbf{x}) \\ &= \mathbf{x}^{\mathrm{T}}(\mathbf{W}_{\mathrm{e}}^{\mathrm{T}}\mathbf{C}\mathbf{W}_{\mathrm{e}})\mathbf{x}. \end{aligned} \tag{34}$$

Substituting (33) into (34) gives

$$\begin{aligned} \mathbf{x}'^{\mathrm{T}}\mathbf{C}\mathbf{x}' &= \mathbf{x}^{\mathrm{T}}[(\mathbb{I}_3 - 2\frac{\mathbf{x}_{\mathrm{e}}\mathbf{x}_{\mathrm{e}}^{\mathrm{T}}\mathbf{C}^{\mathrm{T}}}{\mathbf{x}_{\mathrm{e}}^{\mathrm{T}}\mathbf{C}\mathbf{x}_{\mathrm{e}}})^{\mathrm{T}}\mathbf{C}(\mathbb{I}_3 - 2\frac{\mathbf{x}_{\mathrm{e}}\mathbf{x}_{\mathrm{e}}^{\mathrm{T}}\mathbf{C}^{\mathrm{T}}}{\mathbf{x}_{\mathrm{e}}^{\mathrm{T}}\mathbf{C}\mathbf{x}_{\mathrm{e}}})]\mathbf{x} \\ &= \mathbf{x}^{\mathrm{T}}[(\mathbb{I}_3 - 2\frac{\mathbf{C}\mathbf{x}_{\mathrm{e}}\mathbf{x}_{\mathrm{e}}^{\mathrm{T}}}{\mathbf{x}_{\mathrm{e}}^{\mathrm{T}}\mathbf{C}\mathbf{x}_{\mathrm{e}}})(\mathbf{C} - 2\frac{\mathbf{C}\mathbf{x}_{\mathrm{e}}\mathbf{x}_{\mathrm{e}}^{\mathrm{T}}\mathbf{C}^{\mathrm{T}}}{\mathbf{x}_{\mathrm{e}}^{\mathrm{T}}\mathbf{C}\mathbf{x}_{\mathrm{e}}})]\mathbf{x} \\ &= \mathbf{x}^{\mathrm{T}}\mathbf{C}\mathbf{x} \\ &= 0. \end{aligned} \tag{35}$$

Equation (35) implies that any point $\mathbf{x}_e$ outside the conic $\mathbf{C}$ and the corresponding line $\mathbf{l}_e = \mathbf{C}\mathbf{x}_e$ will define a harmonic homology $\mathbf{W}_e$ to which the conic $\mathbf{C}$ will be invariant. As a result, if the silhouette of the surface of revolution is a conic, there will not be a unique solution to the optimization problem of the harmonic homology $\mathbf{W}$ associated with the silhouette, and hence it provides no information on the intrinsic parameters of the camera.

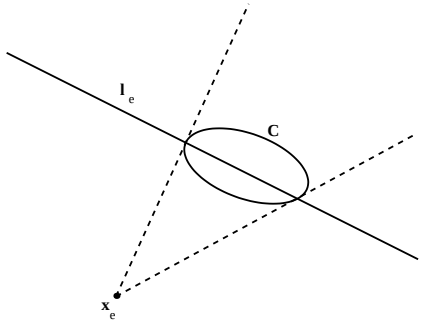

Fig. 11. A conic $\mathbf{C}$ will be invariant to any harmonic homology with a center given by any point $\mathbf{x}_e$ outside the conic, and an axis given by $\mathbf{l}_e = \mathbf{C}\mathbf{x}_e$.

Assume now that the silhouette can be represented as a homogeneous algebraic curve g of degree d [40]. As a result of Bezout's theorem, the silhouette will have $k = 3d(d-2)$ inflection points [41]. If a curve is invariant to a harmonic homology $\mathbf{W}$, its inflection points, which are projective invariants, will be mapped to each other by $\mathbf{W}$. If $d \geq 3$, there will be $k \geq 9$ inflection points, providing at least four matches for computing the harmonic homology. Observe that this result is valid even when the inflection points are imaginary, since there is no problem in mapping an imaginary inflection point to an also imaginary counterpart by a real harmonic homology. The result also holds when the inflection points have multiplicity greater than one, because then the derivatives of g at the inflection point will also be preserved by $\mathbf{W}$. As a result, if $d \geq 3$ and the matching of the inflection points is known, the harmonic homology can be determined. If the matching of the inflection points is not known, there will be at most a finite number of solutions, for different choices in the matching. In general, it should be possible to choose the correct $\mathbf{W}$ by validating it against the rest of the curve. The discussion above demonstrates that conics are the only general (i.e., not for a particular view of a particular example) degeneracy in the computation of the harmonic homology when the silhouette is in the class of homogeneous algebraic curves. It is worthwhile noting that any curve that admits a rational parameterization,

such as B-splines and NURBS, can be expressed in homogeneous algebraic form [42], and therefore the proof is also valid in these particular cases.

B. Vanishing Point at Infinity

When the camera is pointing towards the revolution axis of the surface, the silhouette will exhibit bilateral or skew symmetry (see Section III-C), and the vanishing point $\mathbf{v}_x$ will be at infinity (i.e., $v_3 = 0$). In this situation, the line $\mathbf{l}_x$, on which the principal point is constrained to lie, cannot be determined, and this may cause the calibration equations to be under constrained.

To simplify the analysis, consider a camera with zero skew and unit aspect ratio. Assume now that one homology $\mathbf{W}(\mathbf{v}_x, \mathbf{l}_\mathrm{s})$ with $v_3 \neq 0$ is available. If a second homology $\mathbf{W}(\mathbf{v}'_x, \mathbf{l}'_\mathrm{s}) \neq \mathbf{W}(\mathbf{v}_x, \mathbf{l}_\mathrm{s})$ is also available, there will then be four distinct possibilities for the computation of the principal point $\mathbf{x}_0$ and the focal length f:

(i) $v'_3 \neq 0$ and $\mathbf{l}_x \neq \mathbf{l}'_x$: there will be a unique solution for $\mathbf{x}_0$, given by $\mathbf{x}_0 = \mathbf{l}_x \times \mathbf{l}'_x$.

(ii) $v'_3 \neq 0$ and $\mathbf{l}_x = \mathbf{l}'_x$: there will be exactly one solution for $\mathbf{x}_0$ such that $\mathbf{l}_x^\mathrm{T}\mathbf{x}_0 = 0$ satisfying $f^2 = \mathrm{dist}(\mathbf{x}_0, \mathbf{v}_x) \times \mathrm{dist}(\mathbf{x}_0, \mathbf{l}_\mathrm{s}) = \mathrm{dist}(\mathbf{x}_0, \mathbf{v}'_x) \times \mathrm{dist}(\mathbf{x}_0, \mathbf{l}'_\mathrm{s})$.

(iii) $v'_3 = 0$ and $\mathbf{l}_x \neq \mathbf{l}'_\mathrm{s}$: note that the principal point is now constrained to lie on $\mathbf{l}'_\mathrm{s}$, and there will be a unique solution for $\mathbf{x}_0$, given by $\mathbf{x}_0 = \mathbf{l}_x \times \mathbf{l}'_\mathrm{s}$.

(iv) $v'_3 = 0$ and $\mathbf{l}_x = \mathbf{l}'_\mathrm{s}$: there will be infinite number of solutions for $\mathbf{x}_0$.

The discussion above demonstrates that whenever there are two distinct homologies $\mathbf{W}$ and $\mathbf{W}'$ such that both v_3 and v'_3 are not equal to zero, the computation of the principal point and therefore of the focal length is possible. Moreover, even when there is only one homology with $v_3 \neq 0$, the computation of the principal point and the focal length is still possible, as long as the highly unlikely condition that $\mathbf{l}_x = \mathbf{l}'_\mathrm{s}$ does not occur. When the camera is pointing towards the revolution axis in all images (i.e., $v_3 = 0\ \forall \mathbf{v}_x$), then only the principal point can be estimated.

VII. Error Analysis

A. Proportionality of the Error with the Focal Length

Experiments show that in estimating the harmonic homology $\mathbf{W}$ associated with the silhouette ρ of a surface of revolution, the uncertainty is essentially in the vanishing point $\mathbf{v}_x$. Since $\mathbf{v}_x$ is, in general, tens of thousands of pixels away from the axis $\mathbf{l}_\mathrm{s}$, its error in a direction orthogonal to $\mathbf{l}_\mathrm{s}$ can be neglected in the computation of the principal point and focal length. On the other hand,

the error of $\mathbf{v}_x$ in a direction parallel to $\mathbf{l}_\mathrm{s}$ will lead to the same error in the estimated principal point $\mathbf{x}_0$. This is due to the fact that, under the assumption of zero skew and unit aspect ratio, $\mathbf{x}_0$ must lie on the line $\mathbf{l}_x$ passing through $\mathbf{v}_x$ and orthogonal to $\mathbf{l}_\mathrm{s}$ (see Section IV).

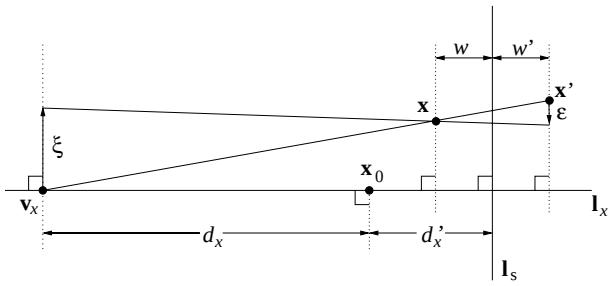

Fig. 12. Error analysis in the estimation of the principal point as the focal length varies.

Fig. 12 shows a point $\mathbf{x}$ in ρ which is transformed by $\mathbf{W}$ to its symmetric counterpart $\mathbf{x}'$ in ρ. If $\mathbf{v}_x$ has an error ξ in a direction parallel to $\mathbf{l}_\mathrm{s}$, then the transformed point will have an error ε (see fig. 12). It is easy to see that ξ and ε are related to each other by

$$\frac{\xi}{\varepsilon} = \frac{d_x + d'_x - w}{w + w'}. \tag{36}$$

Since $d_x = f^2/d'_x$ is much greater than d'_x, w and w', and that w and w' have nearly the same value, equation (36) can be rewritten as

$$\frac{\xi}{\varepsilon} \simeq \frac{f^2}{2d'_x w} = \frac{f}{2\tan\psi w}, \tag{37}$$

where ψ is the angle between the optical axis and the plane Π_s, and $d'_x = f\tan\psi$. Equation (37) implies that if ψ, w and ε are assumed to be approximately constant, then the error ξ of $\mathbf{v}_x$, and hence the error of the principal point $\mathbf{x}_0$, in a direction parallel to $\mathbf{l}_\mathrm{s}$, will be proportional to f. This might limit the usefulness of the technique to wide angle cameras.

B. Validation of the Error Analysis

To validate the error analysis described in the previous subsection, a simple experiment was performed. Four coplanar points configured into a square were placed in front of a camera with zero skew, unit aspect ratio and variable focal length. Initially, the image plane of the camera was parallel to the square formed by these four points, and the optical axis of the camera passed through the center of this square. The camera was then rotated about its optical center and away from the symmetry plane of the four points, distorting the otherwise bilaterally symmetric image

to one invariant to a harmonic homology with the vanishing point at a finite position. Gaussian noise was then added to the coordinates of the projected points, and the corresponding harmonic homology was computed. One can easily relate the parameters in this experiment with those in equation (37): ε is the standard deviation of the noise (i.e., noise level), ψ is the angle by which the camera was rotated from the symmetry plane prior to the projection of the points, and w was taken as the average distance from the points to $\mathbf{l}_s$. It is important to notice that w changes as the focal length changes, thus introducing a nuisance factor that will hide the true linear dependency between the magnitude of the focal length and the error in the position of the principal point. To compensate for that, the optical center of the camera was translated according to the value of the focal length (i.e., the larger the focal length, the further away from the four points the camera was placed), keeping the average value of w constant. Intuitively, this has the effect of maintaining the size of the calibration object (in this case, the four points) approximately constant in the image, despite the changes in the focal length. This experiment was repeated one hundred times for each noise level, and the average norm of the errors in the position of the principal point is shown in fig. 13, as a function of the focal length. The linear relationship described in equation (37) clearly holds, and the proportionality of the error with the noise level σ is also apparent.

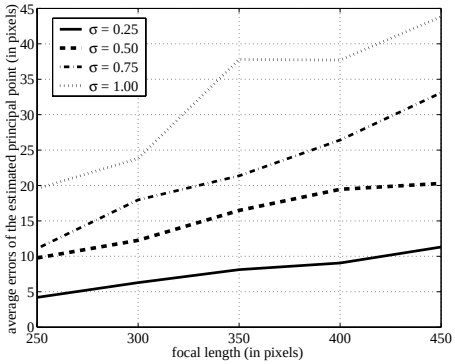

Fig. 13. Linear dependency between the error in the position of the principal point and the magnitude of the focal length. Each point on each curve is the average norm of the errors in the position of the principal point over one hundred experiments.

VIII. Experiments and Results

Experiments on both synthetic and real data were carried out, and the results are presented in the following subsections. In both cases, the cameras were assumed to have zero skew.

A. Synthetic Data

A.1 Generation of Data

The experimental setup consisted of a surface of revolution viewed by a synthetic camera at three different positions, as shown in fig. 14. The synthetic images had a dimension of 640×480 pixels, and the intrinsic parameters of the synthetic camera were given by the calibration matrix

$$\mathbf{K} = \begin{bmatrix} f & 0 & 320 \\ 0 & f & 240 \\ 0 & 0 & 1 \end{bmatrix} \text{ where } f = 700, 1400. \tag{38}$$

The surface of revolution was composed of two spheres intersecting each other. Each sphere was represented by a 4×4 symmetric matrix $\mathbf{Q}_i$ whose projection was given by [43]

$$\mathbf{C}_{ij} = (\mathbf{P}_j \mathbf{Q}_i^{-1} \mathbf{P}_j^{\mathrm{T}})^{-1}, \tag{39}$$

where $\mathbf{P}_j$ was a 3×4 projection matrix and $\mathbf{C}_{ij}$ was a 3×3 symmetric matrix representing the conic, which was the projection of $\mathbf{Q}_i$ in $\mathbf{P}_j$. The silhouette of the surface of revolution in each image was found by projecting each sphere $\mathbf{Q}_i$ onto the image j as the conic $\mathbf{C}_{ij}$ and finding points on each conic that lie outside the other conic. The silhouettes in the three images taken by the synthetic camera with $f = 700$ are shown in fig. 15.

In order to evaluate the robustness of the algorithms described in Section V, uniform random noise was added to each silhouette. Each point in the silhouette was perturbed in a direction normal to the local tangent, and the magnitudes of the noise were smoothed by a Gaussian filter so as to avoid unrealistic jaggedness along the silhouette (see fig. 16).

A.2 Results on Synthetic Data

Experiments on the synthetic data with seven different noise levels were carried out. The seven noise levels were 0.5, 0.7, 1.0, 1.2, 1.5, 1.7 and 2.0 pixels respectively. The noise level for typical real images ranges from 0.7 to 1.5 pixels, and the distortion of the silhouette will be too

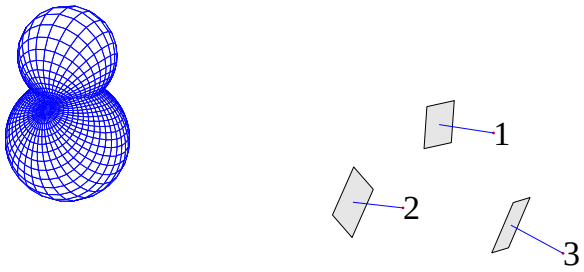

Fig. 14. The experimental setup consisted of a surface of revolution, which was composed of two intersecting spheres, viewed by a synthetic camera at three different positions.

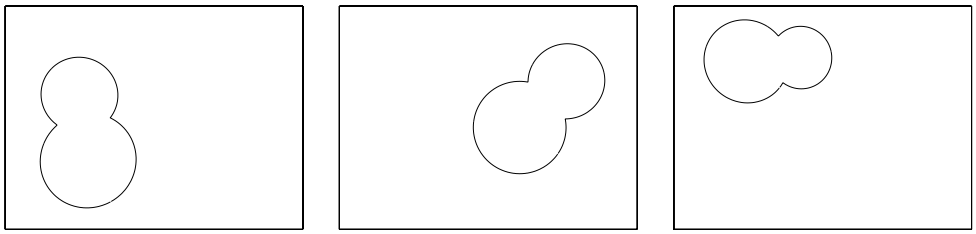

Fig. 15. Silhouettes of the surface of revolution in the three images taken by the synthetic camera with $f = 700$.

great to be realistic when the noise level is above 2.0 pixels. For each noise level, one hundred experiments were conducted using the algorithms described in Section V. In the estimation of the harmonic homology, the number of sample points used was 100. Both method I and II described in Section V-B were used for the computation of the intrinsic parameters.

The experimental results are presented in table I, which shows the root-mean-square (rms) errors of the estimated intrinsic parameters. Note that the values listed in the table have been normalized and are the percentage errors relative to the corresponding ground truth focal lengths. It can be seen from table I that the focal lengths obtained using method II were better than those obtained using method I, regardless of whether the unit aspect ratio constraint was imposed or not. For different versions of method II (i.e., IIa with free aspect ratio and IIb with unit aspect ratio), IIb gave the best results. This is consistent with the well-known fact that the enforcement of known constraints gives more accurate results in camera calibration. Observe that this does not contradict the fact that method IIa gave better results than method I, for in this case different algorithms are being compared. As the noise level increased, the relative errors in the estimated

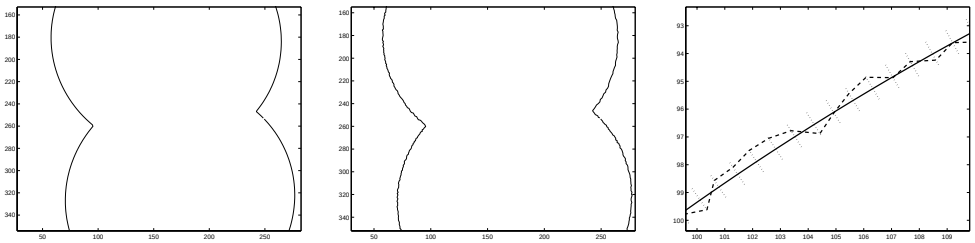

(a) (b) (c)

Fig. 16. (a) The original silhouette. (b) The resultant silhouette after uniform random noise of maximum 0.5 pixels being added. (c) The noise-free and noisy silhouettes are represented by solid and dash lines respectively, and the dotted lines indicate the bounds for noise along the normal direction of each point.

intrinsic parameters increased. Table I also shows that the errors increased with the focal length of the camera (see also fig. 17), and this agrees with the error analysis presented in Section VII. For a noise level of 2.0 pixels, the errors in the estimated focal lengths were less than 6.0% and 7.5% for the synthetic cameras with $f = 700$ and $f = 1400$ respectively.

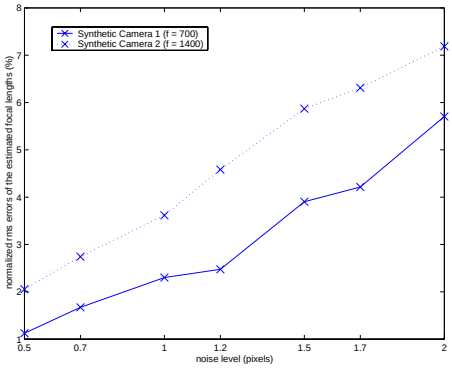

Fig. 17. Normalized rms errors of the estimated focal lengths obtained using method IIb under different noise levels.

B. Real Data

B.1 The Ground Truth

The camera used in the real data experiments was a digital camera with a resolution of 640×480 pixels. The ground truth for the intrinsic parameters of the camera was obtained using a calibration grid. Six images of a calibration grid were taken with the camera at different orientations (see fig. 18). Corner features were extracted from each image using a Canny edge detector [36] and line fitting techniques. For each image, the camera was calibrated using the

TABLE I

EXPERIMENTAL RESULTS OF CALIBRATION FROM SILHOUETTES UNDER DIFFERENT FOCAL LENGTHS AND NOISE LEVELS.

		Synthetic Camera 1 ($f = 700$)				Synthetic Camera 2 ($f = 1400$)			
		Percentage Errors (%)				Percentage Errors (%)			
noise lv	method	f_u	f_v	u_0	v_0	f_u	f_v	u_0	v_0
0.5	I	1.1921	1.1921	0.6325	0.3354	2.2382	2.2382	0.7371	0.4008
0.5	IIa	1.1516	1.0945	0.6023	0.7591	2.0834	2.0280	0.6254	0.8150
0.5	IIb	1.1254	1.1254	0.5687	0.7462	2.0541	2.0541	0.6108	0.8082
0.7	I	1.7181	1.7181	0.8986	0.4725	3.1868	3.1868	1.1699	0.5610
0.7	IIa	1.7111	1.6250	0.8417	1.0659	2.7825	2.7070	1.0280	1.2551
0.7	IIb	1.6711	1.6711	0.7937	1.0478	2.7423	2.7423	1.0052	1.2454
1.0	I	2.4277	2.4277	1.3113	0.7239	4.3078	4.3078	1.8183	0.9197
1.0	IIa	2.3610	2.2334	1.2908	1.6372	3.6626	3.5731	1.2814	1.5222
1.0	IIb	2.3007	2.3007	1.2184	1.6064	3.6161	3.6161	1.2513	1.5134
1.2	I	3.0194	3.0194	1.7414	0.8761	5.5788	5.5788	1.7734	1.0189
1.2	IIa	2.5415	2.4044	1.5292	2.1493	4.6212	4.5503	1.4714	1.7224
1.2	IIb	2.4749	2.4749	1.4469	2.1164	4.5831	4.5831	1.4401	1.7127
1.5	I	4.5876	4.5876	2.7362	1.3309	6.2149	6.2149	1.9063	1.5326
1.5	IIa	4.0019	3.8079	2.0678	3.1898	5.9250	5.8213	1.7284	2.1655
1.5	IIb	3.9031	3.9031	1.9597	3.1490	5.8700	5.8700	1.6910	2.1504
1.7	I	5.6534	5.6534	3.1541	1.7898	8.0902	8.0902	2.9027	1.4357
1.7	IIa	4.3192	4.1158	2.1550	3.7542	6.4024	6.2320	1.8617	2.3701
1.7	IIb	4.2144	4.2144	2.0343	3.7192	6.3107	6.3107	1.8216	2.3488
2.0	I	6.7864	6.7864	4.3649	3.4956	8.8957	8.8957	2.6345	1.9192
2.0	IIa	5.8438	5.6100	3.1055	5.3920	7.2582	7.1219	2.1700	2.3457
2.0	IIb	5.7052	5.7052	2.9625	5.3566	7.1867	7.1867	2.1304	2.3292

method IIa : method II without the unit aspect ratio constraint

method IIb : method II with the unit aspect ratio constraint

DLT technique [19] followed by an optimization which minimized the reprojection errors of the corner features [1], [6]. The results of calibration from the calibration grid are shown in table II.

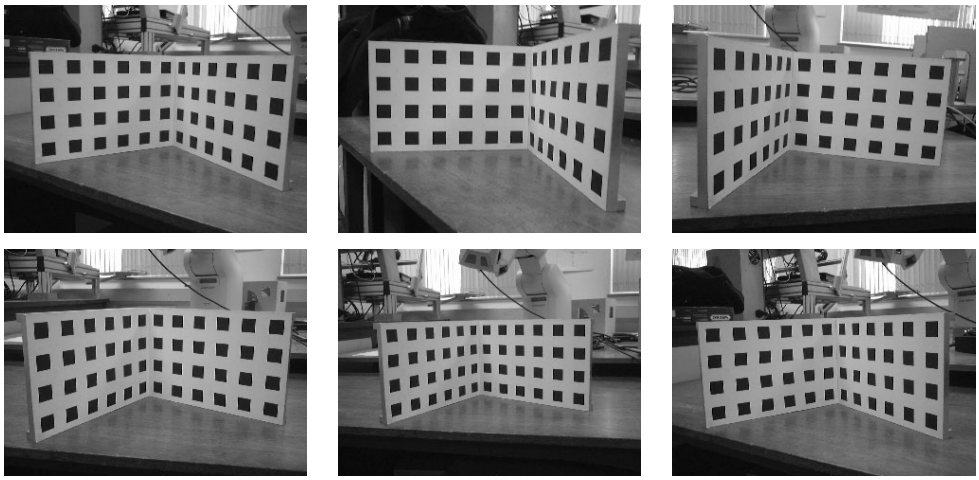

Fig. 18. Six images of a calibration grid taken by the digital camera for calibration.

TABLE II

RESULTS OF CALIBRATION FROM THE SIX IMAGES OF THE CALIBRATION GRID.

assumption: zero skew and unit aspect ratio				
	f_u	f_v	u_0	v_0
mean	687.92	687.92	320.98	230.88
std	1.90	1.90	4.00	3.35
assumption: zero skew				
	f_u	f_v	u_0	v_0
mean	687.70	688.09	320.98	230.88
std	1.83	2.10	4.00	3.34

(all units are in pixels)

B.2 Results on Real Data

Two sets of real images of surfaces of revolution were used for the calibration of the digital camera. The first set consisted of three images of two bowls, which provided four silhouettes for camera calibration (see fig. 19). The second set consisted of eight images of a candle holder, which provided eight silhouettes for camera calibration (see fig. 20). The results of calibration from the two image sets are shown in table III, and table IV shows the percentage errors of the

estimated intrinsic parameters relative to the ground truth focal lengths. Similar to the results of the synthetic experiments, the intrinsic parameters obtained in the real data experiments using method II were better than those obtained using method I. The focal lengths estimated from both the bowls set and the candle holder set (using method II with unit aspect ratio constraint) had an error of only around 3% relative to the ground truth focal length. Fig. 19 and 20 show the extracted silhouettes and the estimated images of the revolution axis. Fig. 21 shows the lines $\mathbf{l}_{xi}$ passing through the corresponding vanishing point $\mathbf{v}_{xi}$ and orthogonal to the corresponding image of the revolution axis $\mathbf{l}_{si}$.

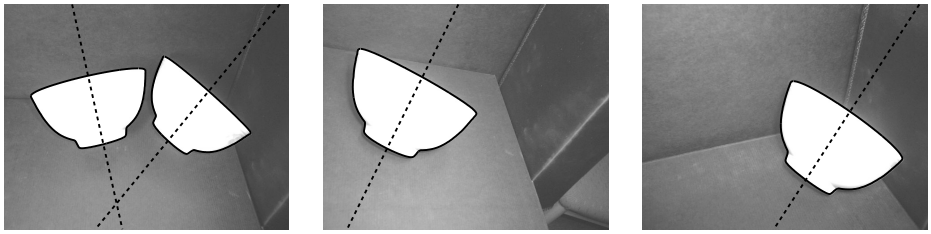

Fig. 19. Three images of two bowls with the extracted silhouettes and estimated images of the revolution axis plotted in solid and dash lines respectively.

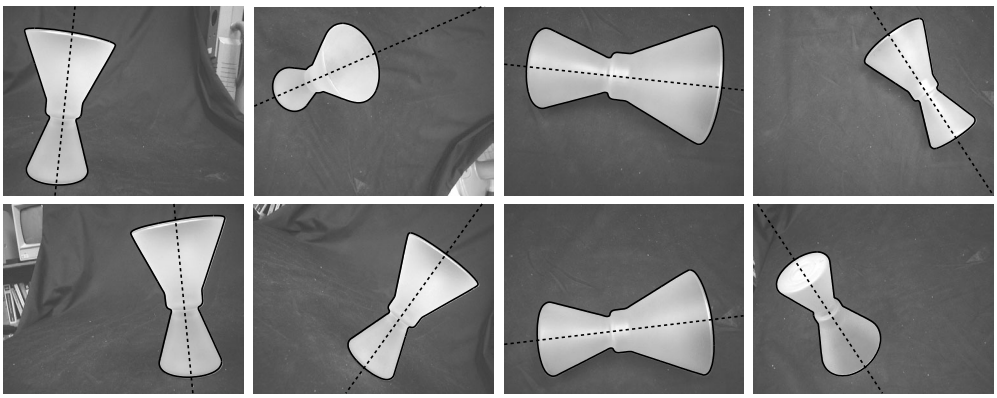

Fig. 20. Eight images of a candle holder with the extracted silhouettes and estimated images of the revolution axis plotted in solid and dash lines respectively.

From table III and table IV, it can be seen that the intrinsic parameters estimated from the candle holder set were slightly better than those from the bowls set. This can be explained as the silhouettes in the candle holder set showed much greater perspective effect than those in the bowls set (see fig. 19 and fig. 20). Besides, the candle holder set also provided more silhouettes, and hence more constraints, than the bowls set for the estimation of the intrinsic parameters.

TABLE III

RESULTS OF CALIBRATION FROM THE BOWLS AND CANDLE HOLDER SETS.

image set	method	f_u	f_v	u_0	v_0
bowls	I	727.12	727.12	332.34	227.21
bowls	IIa	706.65	708.55	321.25	246.25
bowls	IIb	708.63	708.63	322.15	244.75
candle holder	I	727.93	727.93	279.21	231.40
candle holder	IIa	708.44	705.47	331.53	231.18
candle holder	IIb	707.40	707.40	330.60	231.54

(all units are in pixels)

TABLE IV

PERCENTAGE ERRORS IN THE RESULTS OF CALIBRATION FROM THE TWO IMAGE SETS.

		Percentage Errors (%)			
image set	method	f_u	f_v	u_0	v_0
bowls	I	5.70	5.70	1.65	0.53
bowls	IIa	2.76	2.97	0.04	2.23
bowls	IIb	3.01	3.01	0.17	2.02
candle holder	I	5.82	5.82	6.07	0.08
candle holder	IIa	3.02	2.53	1.53	0.04
candle holder	IIb	2.83	2.83	1.40	0.10

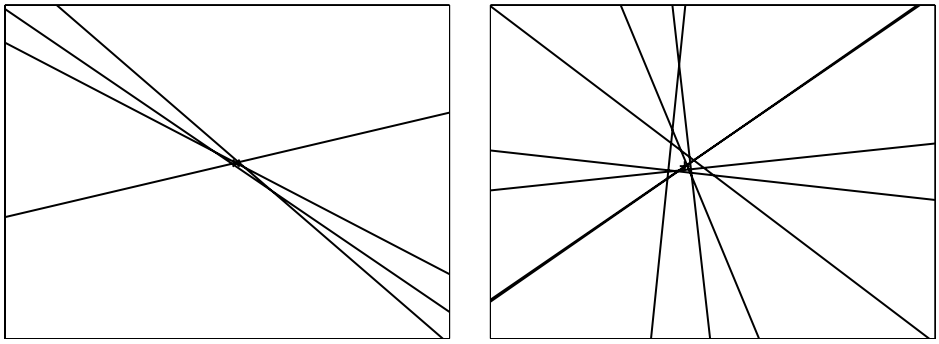

bowls set candle holder set

Fig. 21. The solid lines represent the lines $\mathbf{l}_{xi}$ passing through the corresponding vanishing point $\mathbf{v}_{xi}$ and orthogonal to the corresponding image of the axis revolution $\mathbf{l}_{si}$. Since the principal point $\mathbf{x}_0$ must lie on these lines, it can be estimated as the intersection of two or more lines $\mathbf{l}_{xi}$.

IX. Conclusions

By exploiting the symmetry properties exhibited in the silhouettes of surfaces of revolution and relating them to vanishing points, a practical technique for camera calibration has been developed. The use of surfaces of revolution makes the calibration process easier in not requiring the use of any precisely machined device with known geometry, such as a calibration grid. Besides, a surface of revolution can always be generated by rotating an object of any arbitrary shape around a fixed axis. It means that the calibration technique introduced here can be integrated into a motion estimation and model building system for turntable sequences [44], [28].

Despite the fact that strong perspective effect is required, the method introduced here is promising as demonstrated by the experimental results on both synthetic and real data. The focal lengths were estimated with high accuracy, having an error of only around 3% with respect to the ground truth. Nonetheless, note that neither of the implementations proposed in Section V is statistically optimal, even though the computation of each individual harmonic homology is. The statistically optimal way, which will not be discussed in details here, would be integrating all the information provided by the silhouettes to estimate the intrinsic parameters and the harmonic homologies simultaneously. For a set of N images, this would involve an optimization over a $2N + 4$ parameter space: 4 for the intrinsic parameters, or equivalently, for the image of the absolute conic $\boldsymbol{\omega}$; and $2N$ for the N vanishing points $\mathbf{v}_x$, or equivalently, for the N images of the revolution axes $\mathbf{l}_\mathrm{s}$ (as $\boldsymbol{\omega}\mathbf{v}_x = \mathbf{l}_\mathrm{s}$). This might be included in future work.

Appendix

Definition of the Harmonic Homology

A *perspective collineation* [30], with center $\mathbf{x}_\mathrm{c}$ and axis $\mathbf{l}_\mathrm{a}$, is a collineation which leaves all the lines through $\mathbf{x}_\mathrm{c}$ and points of $\mathbf{l}_\mathrm{a}$ invariant. If the center $\mathbf{x}_\mathrm{c}$ and the axis $\mathbf{l}_\mathrm{a}$ are not incident, the perspective collineation is called a *homology* [30]; otherwise it is called an *elation* [30]. Consider a point $\mathbf{x}$ which is mapped by a homology with center $\mathbf{x}_\mathrm{c}$ and axis $\mathbf{l}_\mathrm{a}$ to the point $\mathbf{x}'$. Let $\mathbf{x}'_\mathrm{c}$ be the point of intersection between the axis $\mathbf{l}_\mathrm{a}$ and a line passing through the points $\mathbf{x}$ and $\mathbf{x}'$. The homology is said to be harmonic if the points $\mathbf{x}$ and $\mathbf{x}'$ are harmonic conjugates with respect to $\mathbf{x}_\mathrm{c}$ and $\mathbf{x}'_\mathrm{c}$ (i.e., the cross-ratio $\{\mathbf{x}_\mathrm{c},\mathbf{x}'_\mathrm{c};\mathbf{x},\mathbf{x}'\}$ equals -1). The matrix $\mathbf{W}$ representing a *harmonic homology* [30] with center $\mathbf{x}_\mathrm{c}$ and axis $\mathbf{l}_\mathrm{a}$, in homogeneous coordinates, is given by

$\mathbf{W} = \mathbb{I}_3 - 2\frac{\mathbf{x}_c \mathbf{l}_a^T}{\mathbf{x}_c^T \mathbf{l}_a}$. More details on harmonic homology can be found in [29], [30].

REFERENCES

[1] O. D. Faugeras and G. Toscani, "The calibration problem for stereo," in *Proc. Conf. Computer Vision and Pattern Recognition*, Miami, FL, June 1986, pp. 15–20.

[2] R. Y. Tsai, "A versatile camera calibration technique for high-accuracy 3D machine vision metrology using off-the-shelf tv cameras and lenses," *IEEE Trans. Robotics and Automation*, vol. 3, no. 4, pp. 323–344, August 1987.

[3] R. K. Lenz and R. Y. Tsai, "Techniques for calibration of the scale factor and image center for high accuracy 3D machine vision metrology," *IEEE Trans. on Pattern Analysis and Machine Intelligence*, vol. 10, no. 5, pp. 713–720, September 1988.

[4] Z. Zhang, "A flexible new technique for camera calibration," *IEEE Trans. on Pattern Analysis and Machine Intelligence*, vol. 22, no. 11, pp. 1330–1334, November 2000.

[5] R. I. Hartley and A. Zisserman, *Multiple View Geometry in Computer Vision*, Cambridge University Press, Cambridge, UK, 2000.

[6] O. D. Faugeras, *Three-Dimensional Computer Vision: a Geometric Viewpoint*, MIT Press, Cambridge, MA, 1993.

[7] B. Caprile and V. Torre, "Using vanishing points for camera calibration," *Int. Journal of Computer Vision*, vol. 4, no. 2, pp. 127–140, March 1990.

[8] R. Cipolla, T. W. Drummond, and D. Robertson, "Camera calibration from vanishing points in images of architectural scenes," in *Proc. British Machine Vision Conference*, T. Pridmore and D. Elliman, Eds., Nottingham, UK, September 1999, vol. 2, pp. 382–391.

[9] D. Liebowitz and A. Zisserman, "Combining scene and auto-calibration constraints," in *Proc. 7th Int. Conf. on Computer Vision*, Corfu, Greece, September 1999, pp. 293–300.

[10] A. Zisserman, D. Forsyth, J. L. Mundy, and C. A. Rothwell, "Recognizing general curved objects efficiently," in *Geometric Invariance in Computer Vision*, J. L. Mundy and A. Zisserman, Eds., Artificial Intelligence Series, chapter 11, pp. 228–251. MIT Press, Cambridge, MA, 1992.

[11] J. Liu, J. L. Mundy, D. A. Forsyth, A. Zisserman, and C. A. Rothwell, "Efficient recognition of rotationally symmetric surface and straight homogeneous generalized cylinders," in *Proc. Conf. Computer Vision and Pattern Recognition*, New York, NY, June 1993, pp. 123–129.

[12] J. L. Mundy and A. Zisserman, "Repeated structures: Image correspondence constraints and 3D structure recovery," in *Applications of Invariance in Computer Vision, Second Joint European - US Workshop*, J. L. Mundy, A. Zisserman, and D. Forsyth, Eds., Ponta Delgada, Azores, Portugal, October 1993, vol. 825 of *Lecture Notes in Computer Science*, pp. 89–106, Springer–Verlag.

[13] A. Zisserman, J. L. Mundy, D. A. Forsyth, J. Liu, N. Pillow, C. Rothwell, and S. Utcke, "Class-based grouping in perspective images," in *Proc. 5th Int. Conf. on Computer Vision*, Cambridge, MA, USA, June 1995, pp. 183–188.

[14] R. W. Curwen, C. V. Stewart, and J. L. Mundy, "Recognition of plane projective symmetry," in *Proc. 6th Int. Conf. on Computer Vision*, Bombay, India, January 1998, pp. 1115–1122.

[15] K.-Y. K. Wong, P. R. S. Mendonça, and R. Cipolla, "Camera calibration from symmetry," in *The Mathematics of Surfaces IX*, R. Cipolla and R. Martin, Eds., Cambridge, UK, September 2000, pp. 214–226, Springer–Verlag.

[16] D. C. Brown, "Close-range camera calibration," *Photogrammetric Engineering*, vol. 37, no. 8, pp. 855–866, August 1971.

[17] I. Sobel, "On calibrating computer controlled cameras for perceiving 3-D scenes," *Artificial Intelligence*, vol. 5, no. 2, pp. 185–198, June 1974.

[18] W. Faig, "Calibration of close-range photogrammetry system: Mathematical formulation," *Photogrammetric Engineering and Remote Sensing*, vol. 41, no. 12, pp. 1479–1486, December 1975.

[19] Y. I. Abdel-Aziz and H. M. Karara, "Direct linear transformation from comparator coordinates into object space coordinates in close-range photogrammetry," in *Proc. ASP/UI Symp. Close-Range Photogrammetry*, Urbana, IL, January 1971, pp. 1–18.

[20] S. J. Maybank and O. D. Faugeras, "A theory of self-calibration of a moving camera," *Int. Journal of Computer Vision*, vol. 8, no. 2, pp. 123–151, August 1992.

[21] Q. T. Luong and O. D. Faugeras, "Self-calibration of a moving camera from point correspondences and fundamental matrices," *Int. Journal of Computer Vision*, vol. 22, no. 3, pp. 261–289, March 1997.

[22] B. Triggs, "Autocalibration and the absolute quadric," in *Proc. Conf. Computer Vision and Pattern Recognition*, San Jaun, PR, June 1997, pp. 609–614.

[23] M. Pollefeys, R. Koch, and L. J. van Gool, "Self-calibration and metric reconstruction inspite of varying and unknown intrinsic camera parameters," *Int. Journal of Computer Vision*, vol. 32, no. 1, pp. 7–25, August 1999.

[24] L. de Agapito, E. Hayman, and I. D. Reid, "Self-calibration of rotating and zooming cameras," *Int. Journal of Computer Vision*, vol. 45, no. 2, pp. 107–127, November 2001.

[25] M. Armstrong, A. Zisserman, and R. Hartley, "Self-calibration from image triplets," in *Proc. 4th European Conf. on Computer Vision*, B. Buxton and R. Cipolla, Eds., Cambridge, UK, April 1996, vol. 1064 of *Lecture Notes in Computer Science*, pp. 3–16, Springer–Verlag.

[26] L. G. Roberts, "Machine perception of three-dimensional solids," in *Optical and Electro-Optical Information Processing*, J. T. Tippett, D. A. Berkowitz, L. C. Clapp, C. J. Koester, and A. Vanderburgh, Jr., Eds., pp. 159–197. MIT Press, 1965.

[27] P. R. S. Mendonça, K.-Y. K. Wong, and R. Cipolla, "Recovery of circular motion from profiles of surfaces," in *Vision Algorithms: Theory and Practice*, B. Triggs, A. Zisserman, and R. Szeliski, Eds., Corfu, Greece, September 1999, vol. 1883 of *Lecture Notes in Computer Science*, pp. 151–167, Springer–Verlag.

[28] P. R. S. Mendonça, K.-Y. K. Wong, and R. Cipolla, "Epipolar geometry from profiles under circular motion," *IEEE Trans. on Pattern Analysis and Machine Intelligence*, vol. 23, no. 6, pp. 604–616, June 2001.

[29] J. G. Semple and G. T. Kneebone, *Algebraic Projective Geometry*, Oxford Classic Texts in the Physical Sciences. Clarendon Press, Oxford, UK, 1998, Originally published in 1952.

[30] H. S. M. Coxeter, *Introduction to Geometry*, Wiley and Sons, New York, 2^{nd} edition, 1989.

[31] J. R. Kender and Kanade, "Mapping image properties into shape constraints: Skewed symmetry, affine-transformable patterns, and the shape-from-texture paradigm," in *Human and Machine Vision*, J. Beck, B. Hope, and A. Rosenfeld, Eds., pp. 237–257. Academic Press, New York, 1983.

[32] D. P. Mukherjee, A. Zisserman, and J. M. Brady, "Shape from symmetry–detecting and exploiting symmetry in affine images," *Phil. Trans. Royal Soc. London A*, vol. 351, pp. 77–106, 1995.

[33] T. J. Cham and R. Cipolla, "Geometric saliency of curve correspondences and grouping of symmetric contours," in *Proc. 4th European Conf. on Computer Vision*, B. Buxton and R. Cipolla, Eds., Cambridge, UK, April 1996, vol. 1064 of *Lecture Notes in Computer Science*, pp. 385–398, Springer–Verlag.

[34] J. Sato and R. Cipolla, "Affine integral invariants for extracting symmetry axes," *Image and Vision Computing*, vol. 15, no. 8, pp. 627–635, August 1997.

[35] A. Zisserman, D. Liebowitz, and M. Armstrong, "Resolving ambiguities in auto-calibration," *Phil. Trans. Royal Soc. London A*, vol. 356, no. 1740, pp. 1193–1211, 1998.

[36] J. Canny, "A computational approach to edge detection," *IEEE Trans. on Pattern Analysis and Machine Intelligence*, vol. 8, no. 6, pp. 679–698, November 1986.

[37] M. Wright, A. W. Fitzgibbon, P. J. Giblin, and R. B. Fisher, "Convex hulls, occluding contours, aspect graphs and the hough transform," *Image and Vision Computing*, vol. 14, no. 8, pp. 627–634, August 1996.

[38] R. Glacahet, M. Dhome, and J. T. Lapreste, "Finding the perspective projection of an axis of revolution," in *Pattern Recognition Letters*, November 1991, vol. 12, pp. 693–700.

[39] W. H. Press, S. A. Teukolsky, W. T. Vetterling, and B. P. Flannery, *Numerical Recipes in C : The Art of Scientific Computing*, Cambridge University Press, Cambridge, UK, 2 edition, January 1993.

[40] F. Kirwan, *Complex Algebraic Curves*, vol. 23 of *London Mathematical Society Student Texts*, Cambridge University Press, Cambridge, UK, 1992.

[41] Plücker, J., *System der analytischen Geometrie : auf neue Betrachtungsweisen gegrundet und insbesonderer eine ausfuhrliche Theorie der Curven dritter Ordnung enthaltend*, Berlin, 1835.

[42] T. W. Sederberg, D. C. Anderson, and R. N. Goldman, "Implicit representation of parametric curves and surfaces," *Computer Vision, Graphics and Image Processing*, vol. 28, no. 1, pp. 72–84, October 1984.

[43] G. Cross and A. Zisserman, "Quadric reconstruction from dual-space geometry," in *Proc. 6th Int. Conf. on Computer Vision*, Bombay, India, January 1998, pp. 25–31.

[44] A. W. Fitzgibbon, G. Cross, and A. Zisserman, "Automatic 3D model construction for turn-table sequences," in *3D Structure from Multiple Images of Large-Scale Environments, European Workshop SMILE'98*, R. Koch and L. Van Gool, Eds., Freiburg, Germany, June 1998, vol. 1506 of *Lecture Notes in Computer Science*, pp. 155–170, Springer–Verlag.